

UC Santa Cruz

UC Santa Cruz Previously Published Works

Title

The Emerging Layered Hydroxide Plates with Record Thickness for Enhanced High-Mass-Loading Energy Storage

Permalink

<https://escholarship.org/uc/item/2wf695qd>

Journal

Advanced Materials, 35(19)

ISSN

0935-9648

Authors

Guo, Wei

Dun, Chaochao

Marcus, Matthew A

et al.

Publication Date

2023-05-01

DOI

10.1002/adma.202211603

Peer reviewed

The Emerging Layered Hydroxide Plates with Record Thickness for Enhanced High-Mass-Loading Energy Storage

Wei Guo, Chaochao Dun, Matthew A. Marcus, Victor Venturi, Zack Gainsforth, Feipeng Yang, Xuefei Feng, Venkatasubramanian Viswanathan, Jeffrey J. Urban, Chang Yu,* Qiuyu Zhang,* Jinghua Guo,* and Jieshan Qiu*

The past decade has witnessed the development of layered-hydroxide-based self-supporting electrodes, but the low active mass ratio impedes its all-around energy-storage applications. Herein, the intrinsic limit of layered hydroxides is broken by engineering F-substituted β -Ni(OH)₂ (Ni–F–OH) plates with a sub-micrometer thickness (over 700 nm), producing a superhigh mass loading of 29.8 mg cm⁻² on the carbon substrate. Theoretical calculation and X-ray absorption spectroscopy analysis demonstrate that Ni–F–OH shares the β -Ni(OH)₂-like structure with slightly tuned lattice parameters. More interestingly, the synergy modulation of NH₄⁺ and F⁻ is found to serve as the key enabler to tailor these sub-micrometer-thickness 2D plates thanks to the modification effects on the (001) plane surface energy and local OH⁻ concentration. Guided by this mechanism, the superstructures of bimetallic hydroxides and their derivatives are further developed, revealing they are a versatile family with great promise. The tailored ultrathick phosphide superstructure achieves a superhigh specific capacity of 7144 mC cm⁻² and a superior rate capability (79% at 50 mA cm⁻²). This work highlights a multiscale understanding of how exceptional structure modulation happens in low-dimensional layered materials. The as-built unique methodology and mechanisms will boost the development of advanced materials to better meet future energy demands.

1. Introduction

Electrochemical energy storage techniques have attracted intense attention over the last few decades.^[1–3] Among them, hybrid supercapacitors (HSCs), which comprise a battery-type electrode and a capacitive-type electrode with the synergistic mechanism of surface reaction- and bulky diffusion-controlled chemistries, feature integrated advantages of high safety, superior energy, and power densities for future commercialization.^[4–6] Significant efforts have been devoted to tailoring advanced electrode materials of HSCs with enhanced reaction dynamics and intrinsic reactivity. Specifically, transition-metal-based 2D layered hydroxides and their derivatives with high theoretical capacity and structure tunability have been recognized as a sound choice of battery-type electrodes.^[7–11] However, due to the low mass ratio of active materials within the whole cell (including

W. Guo, C. Yu, J. Qiu
State Key Lab of Fine Chemicals
School of Chemical Engineering
Liaoning Key Lab for Energy Materials and Chemical Engineering
Dalian University of Technology
Dalian 116024, P. R. China
E-mail: chang.yu@dlut.edu.cn; jqiu@dlut.edu.cn

W. Guo, Q. Zhang
School of Chemistry and Chemical Engineering
Key Laboratory of Special Functional and Smart Polymer Materials of
Ministry of Industry and Information Technology
Northwestern Polytechnical University
Xi'an 710072, P. R. China
E-mail: qzhang@nwpu.edu.cn


W. Guo, M. A. Marcus, F. Yang, X. Feng, J. Guo
Advanced Light Source
Lawrence Berkeley National Laboratory
Berkeley, CA 94720, USA
E-mail: jguo@lbl.gov

C. Dun, J. J. Urban
The Molecular Foundry
Lawrence Berkeley National Laboratory
Berkeley, CA 94720, USA

V. Venturi, V. Viswanathan
Department of Mechanical Engineering
Carnegie Mellon University
Pittsburgh, PA 15232, USA

Z. Gainsforth
Space Sciences Laboratory
University of California
Berkeley, Berkeley, CA 94720, USA

V. Viswanathan
Department of Physics
Carnegie Mellon University
Pittsburgh, PA 15232, USA

 The ORCID identification number(s) for the author(s) of this article can be found under <https://doi.org/10.1002/adma.202211603>.

DOI: 10.1002/adma.202211603

active and inactive mass, Equation 1), an undesirable degradation of the real capability appears, serving as a bottleneck for their practical applications.^[12,13]

$$m_{\text{cell}} = m_{\text{active}} + m_{\text{inactive}} \quad (1)$$

Given that, although numerous thin-film electrodes display optimal specific mass capacity (Q_m , generally based on the active mass), practical applications have failed because their mass loading λ ($<3 \text{ mg cm}^{-2}$) is less than 10 mg cm^{-2} which is required for commercial viability.^[14,15] Instead, areal capacity (Q_a , Equation 2), which is related to Q_m and highlights the significance of active mass loading (λ), has been recognized to reflect the real picture of the charge-storage capability.

$$Q_a = \lambda Q_m \quad (2)$$

On top of that, the improved volume fraction (f_c) by increasing λ contributes to the increase of volume energy density (E_{vol}) of the device ($E_{\text{vol-device}}$).^[16,17]

$$E_{\text{vol-device}} = 0.25 f_c \times E_{\text{vol}} \quad (3)$$

Taken together, the development of high-mass-loading electrodes with competitive charge-delivery capability is highly desired to improve energy storage technology.

To attain this goal, scientific design principles must include a comprehensive elucidation of potential thermodynamics and surface/interface reaction barriers. For many traditional electrodes, the slurry-coating procedure entails the introduction of an inactive polymer binder (Figure 1a). This binder not only causes non-negligible “dead mass” with no capacity contribution,^[18,19] but also highly restricts the electrolyte-transport and electron-transfer dynamics. To alleviate this, self-supporting electrodes have been developed in which the active materials grow directly on conductive substrates to form well-defined nanoarrays.^[20–22] Owing to the absence of binders and the strengthened interfacial interaction, electrochemically inert “dead mass” is avoided, allowing the promoted mass and charge-transfer processes as well as reduced internal resistance. However, most of the current nanostructures can only present a low λ on substrates (about 3 mg cm^{-2} , below 20% of the whole electrode mass) and fail to satisfy commercial requirements as we mentioned above.

With transition-metal-based 2D layered hydroxides as a proof-of-concept, we propose a new type of electrode (tailored ultrathick plates on carbon substrate) with increased charge-storage

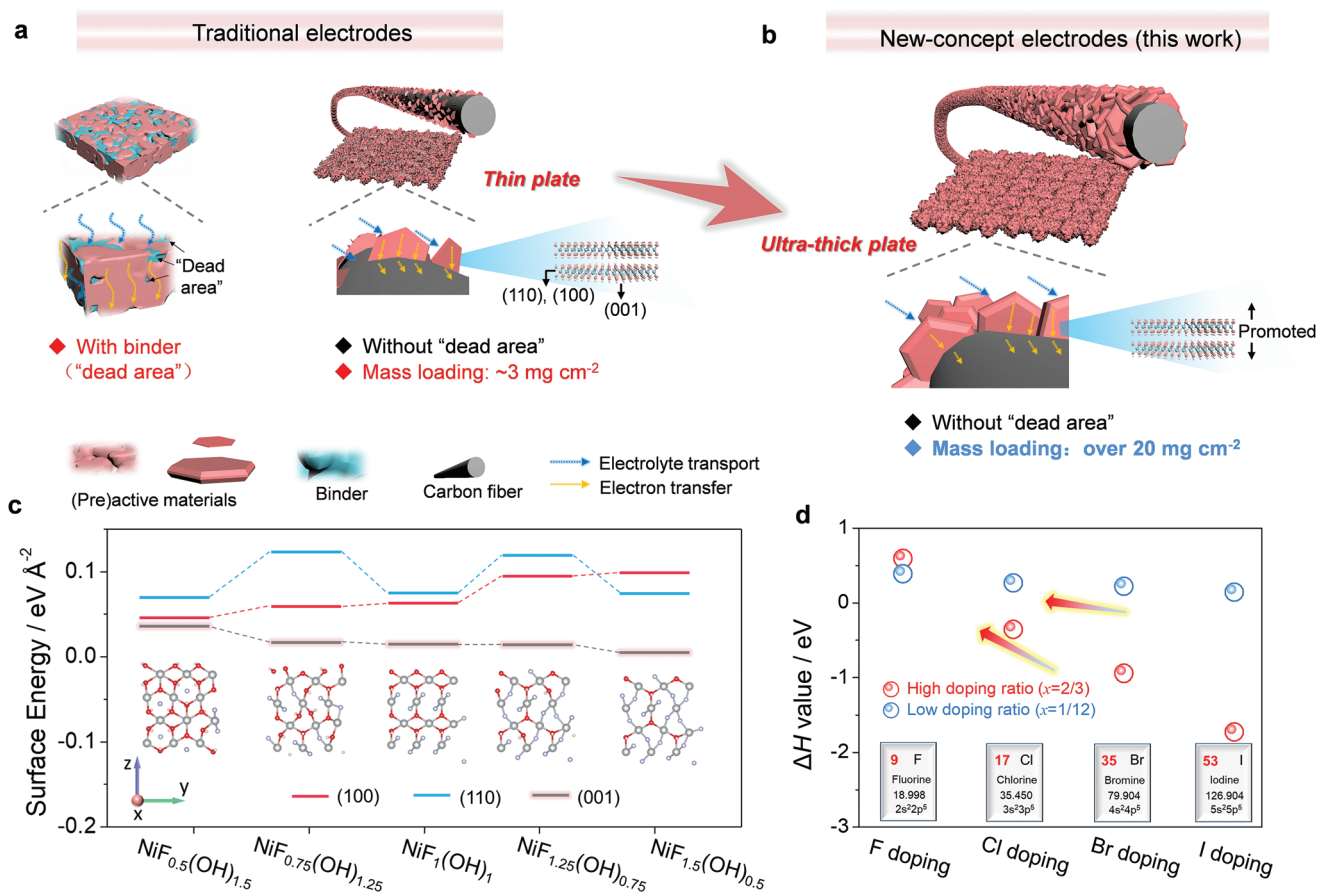


Figure 1. a,b) Schematic illustration of traditional (a) and the new-concept (b) electrodes. c) Calculated surface energies of $\text{NiF}_x(\text{OH})_{2-x}$ for (100), (110), and (001) facets, with the inset showing the slab models for the typical (001) surface after relaxing. d) Decomposition enthalpies for a typical decomposition reaction ($\text{NiX}_x(\text{OH})_{2-x} \rightarrow (1-0.5x)\text{Ni}(\text{OH})_2 + 0.5x\text{NiX}_2$) for $\text{NiX}_x(\text{OH})_{2-x}$ (with $X = \text{F, Cl, Br, or I}$) under different doping ratios.

capability. We focus on the widely adopted β -Ni(OH)₂ as an example, which is generally produced with a thin nanosheet morphology and a low packing density (Figure S1, Supporting Information). Considering the unique low F–F bonding energy (150 kJ mol⁻¹) and high Ni–F bonding energy (440 kJ mol⁻¹) in comparison to those of O–O (498 kJ mol⁻¹) and Ni–O (360 kJ mol⁻¹), we predict that F-doping into β -Ni(OH)₂ is likely to significantly modulate the crystal surface and break the intrinsic limit, holding the promise for realizing the high-mass-loading requirements (Figure 1b).

In this work, for the first time, an NH₄⁺ and F⁻ synergy mechanism is developed to tailor F-substituted β -Ni(OH)₂ (Ni–F–OH) with a sub-micrometer thickness (up to 700 nm) on carbon substrates, realizing a superhigh mass loading of 29.8 mg cm⁻² (up to 72% of the whole electrode mass). Through density functional theory (DFT) calculation and ex situ experimental study, we decouple the fine structure and substantiate the key role of NH₄⁺ and F⁻ modulation: on one hand, F⁻ is thermodynamically favorable to entering the lattice of β -Ni(OH)₂ and tuning the surface energy, thus breaking the growth limit along (001) plane; on the other hand, NH₄⁺ can well balance the local OH⁻ concentration to ensure the phase-holding growth of the large single-crystal Ni–F–OH. More remarkably, we find this NH₄⁺–F⁻ synergy modulation strategy holds a promise to produce a large family of ultra-thick plate superstructures, evidenced by the successful production of a series of ultrathick bimetallic hydroxides and their derivatives. With the ultrathick bimetallic phosphide plates as the (pre)active materials, a record-level areal capacitance of 7144 mC cm⁻² is finely realized with a high retention rate of 79% at 50 mA cm⁻². This work provides a research route for the development of advanced superstructures, responsible for the practical applications of energy-storage devices in the near future.

2. Results and Discussion

2.1. Theoretical Evaluation for Tailoring of the Ni–F–OH Superstructure

It is widely accepted that surface energy serves as the main descriptor for the growth of nanocrystals.^[23–25] To study the potential effect of F-doping, a series of F-substituted β -Ni(OH)₂ (denoted as NiF_x(OH)_{2-x}, or Ni–F–OH) models are investigated. Figure 1c presents the calculated surface energy values of NiF_x(OH)_{2-x} for (100), (110), and (001) facets. The surface energies of (001) surfaces for all cases are consistently smaller than their counterparts, especially with a higher doping level, indicative of the plate-like morphology. The surface energy of (001) facet for pure β -Ni(OH)₂ was also given in Table S1 in the Supporting Information. When compared to that of Ni–F–OH, its low surface energy manifests the increase of thickness when OH⁻ is substituted by F⁻. A thermodynamic analysis, which serves as another important tool to predict novel materials,^[26–28] is also conducted. To gain a comprehensive understanding of the modulation mechanisms, the effects of different types of halogens are considered. Figure 1d displays the decomposition enthalpies for a typical decomposition reaction for NiX_x(OH)_{2-x} (X = F, Cl, Br, and I) under different doping contents (the

detailed models are shown in Figures S2 and S3 in the Supporting Information). The doping of F into β -Ni(OH)₂ is thermodynamically more stable when compared with that of other halogens. Specifically, at a low doping ratio ($x = 1/12$), the decomposition reaction is unfavorable for all halides, especially for F; at a high ratio ($x = 2/3$), the decomposition reaction is even more challenging for F, while it becomes energetically favorable for the other halogens, in particular for Br and I, which have a driving force of 0.9 and 1.7 eV per nickel atom. These results show that F can stably enter into the crystal structure of β -Ni(OH)₂ and modulate the surface energy to a great degree, holding a promise for effectively tailoring advanced ultrathick plate superstructure.

2.2. Decoupling the Formation Process and Mechanism of Ni–F–OH

To better evaluate the nucleation process of Ni–F–OH, the equilibrium constants are studied based on three relevant reactions (Figure S4, Supporting Information). It is found that F sites bonded with Ni tend to be partially substituted by OH⁻ to form traditional Ni(OH)₂ with thin-plate microstructure, in accordance with relevant results in literature.^[29,30] The scanning electron microscopy (SEM) result in Figure 2b demonstrates the developed morphology tuned by Na⁺–F⁻ ion pair. In this case, since local OH⁻ remains excessive, thin nanosheets (namely, Ni–F–OH@Ni(OH)₂) instead of ultrathick plates are observed due to the out-of-control phase separation (Figure 2a). This is further confirmed by our XRD result (Figure S5, Supporting Information) that displays the significant Ni(OH)₂ phase. Considering that, instead of Na⁺, NH₄⁺ with Lewis acid properties,^[31,32] is applied in the presence of F⁻, with an aim to gain the desirable Ni–F–OH microstructure. Figure S5 (Supporting Information) gives the X-ray diffraction (XRD) patterns and SEM images of the as-formed Ni–F–OH samples with different mole ratios of NH₄⁺ to F⁻ from 0:7 to 7:7. As the increase of NH₄⁺, the microstructure is ultimately dominated by the Ni–F–OH phase with high purity, and the plate becomes thicker and thicker (Figure 2c; Figure S5, Supporting Information). That is to say, with a moderate amount of NH₄⁺ as the OH⁻ consumer, the phase-holding nucleation of Ni–F–OH is boosted, leading to the formation of single-crystal ultrathick plates (Figure 2a).

With the above discussions in mind, the formation mechanisms of ultrathick Ni–F–OH plates can be attributed to the NH₄⁺ and F⁻ synergy mechanism with dual modulation effects: (i) modulating the (001) surface energy by F substitution, and (ii) balancing the local OH⁻ concentration with NH₄⁺. As a result, the as-formed Ni–F–OH microstructure on the carbon substrate displays a record sub-micrometer thickness with a considerably improved mass loading (29.8 mg cm⁻², 72% of the whole electrode mass), holding a great promise to serve as the (pre)active materials for commercial energy applications. As shown by the transmission electron microscopy (TEM) image and the corresponding elemental mapping, Ni, F, and O are uniformly distributed on the Ni–F–OH microstructure, further manifesting the successful incorporation of F (Figure 2d,e). The corresponding selected-area electron diffraction (SAED) pattern demonstrates that these well-tailored crystals display

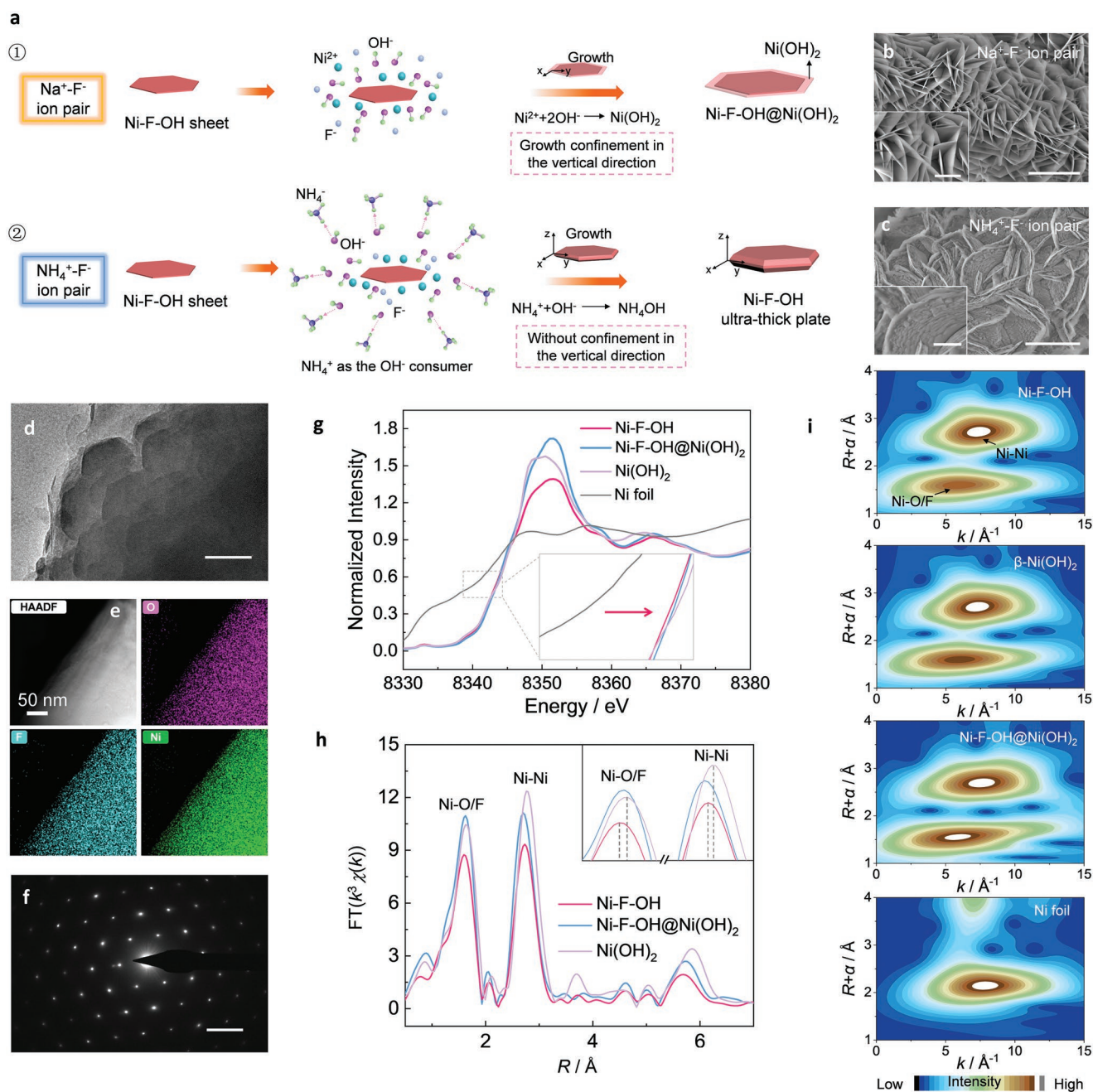


Figure 2. a) Schematic illustration of the synergy modulation effects of NH_4^+ and F^- on the growth of Ni-F-OH. b, c) SEM images of the generated microstructures with $\text{Na}^+\text{-F}^-$ (b) and $\text{NH}_4^+\text{-F}^-$ (c) modulation effects, respectively. Scale bar: 4 μm; scale bar of inset: 1 μm. d) TEM image of Ni-F-OH. Scale bar: 100 nm. e) Elemental mapping images of Ni-F-OH based on aberration-corrected high-resolution electron microscopy. Scale bar: 50 nm. f) SAED pattern of Ni-F-OH. Scale bar: 5 nm⁻¹. g) Ni K-edge XANES spectra of Ni-F-OH, Ni-F-OH@Ni(OH)₂, the Ni foil and standard β-Ni(OH)₂. h) FT-EXAFS spectra of Ni-F-OH, Ni-F-OH@Ni(OH)₂, and standard β-Ni(OH)₂. i) WT-EXAFS maps of Ni-F-OH, Ni-F-OH@Ni(OH)₂, the Ni foil and standard β-Ni(OH)₂.

unidirectionally aligned single-crystal characteristics with a hexagonal symmetry on the (001) surface (Figure 2e).^[33,34] It is proved that the feeding amount of the NH_4^+ and F^- needs to be sufficient to avoid the formation of an undesired phase structure (Figures S6 and S7, Supporting Information).

To further prove the critical role of NH_4^+ and F^- synergy mechanism, a series of contrast experiments are performed

by replacing $\text{NH}_4^+\text{-F}^-$ ion pair with equimolar $\text{NH}_4^+\text{-Cl}^-$, $\text{NH}_4^+\text{-Br}^-$, or $\text{NH}_4^+\text{-I}^-$ ion pairs. Instead of highly crystalline and ultrathick plates like Ni-F-OH, small and low-crystallinity microstructures are observed in these cases (Figure S8, Supporting Information), further confirming the robust incorporation and unique modulation effect of F^- . This is consistent with the theoretical calculations shown in Figure 1c.

2.3. Exploring the Fine Structure of Ni–F–OH and its Versatile Family

To gain more insights into the as-formed Ni–F–OH microstructure, X-ray absorption fine structure (XAFS) characterization was done. From the Ni K-edge X-ray absorption near edge structure (XANES) spectra, we found that the halfway-up point (normalized signal = 0.5 with the post-edge set to 1.0) is almost the same (within 0.2 eV, Figure 2g) for Ni–F–OH, Ni–F–OH@Ni(OH)₂, and β-Ni(OH)₂. This suggests that all of them possess the same Ni²⁺ valence,^[35,36] and F-substitution presents a negligible effect on the valence states of Ni. The Fourier transform (FT) of the extended XAFS (FT-EXAFS) spectra demonstrate that all samples feature three prominent peaks in the Ni K-edge EXAFS $k^3\chi(k)$ oscillation spectra, originating from the Ni–O/F first-neighbor, Ni–Ni second neighbor, and Ni–Ni–Ni paths (Figure S9, Supporting Information), with the oscillations of the imaginary parts tracking closely with each other (Figure 2h).^[37,38] Therefore, it can be concluded that the microstructure of the as-formed Ni–F–OH is similar to that of β-Ni(OH)₂, which is also evidenced by the wave transform (WT) analysis of EXAFS (WT-EXAFS) as shown in Figure 2i. The slight negative shift related to the first two shells (Ni–O/F and Ni–Ni bonding), is attributed to the shorter Ni–O/F and Ni–Ni distances in Ni–F–OH.^[39,40] Given the similarity of the fine structures, we subsequently conducted the fitting with standard β-Ni(OH)₂ as the model, and the fitted distances of Ni–O, Ni–Ni, and Ni–Ni–Ni paths are shown in Table S2 and Figure S10 in the Supporting Information.

It should be noted that, although the XANES and FT-EXAFS results concurrently reveal that the fine structure of Ni–F–OH is similar to that of β-Ni(OH)₂, the corresponding XRD patterns are not exactly the same (Figure S11, Supporting Information). To better understand this phenomenon, we conducted a DFT relaxation simulation of the Ni–F–OH structure from β-Ni(OH)₂. A starting structure with the substitution of F is constructed in Figure S12 (Supporting Information) based on a 3 × 1 × 2 superlattice structure. The generated structure after relaxation (Figure S13, Supporting Information) presents lattice parameters of *a*, *b*, *c* = 9.271, 3.121, 9.351 Å and α , β , γ = 84.31°, 88.53°, 120.07° (Table S3, Supporting Information), respectively. With this relaxed model, the FT-EXAFS spectrum of Ni–F–OH is further fitted (Figure S14, Supporting Information), producing the average Ni–O and Ni–F distances of 2.01 Å (error bar, 0.01 Å) and 2.07 Å (error bar, 0.01 Å), with the Ni–Ni distance determined to be 3.069 Å (error bar, 0.005 Å). The simulated XRD pattern is given in Figure S15 in the Supporting Information, which displays a reasonable agreement with our experimental results except for the two peaks at 39.5° and 41° (indexed to Miller indices (310) and (312), respectively). After applying a displacement of successive layers by 1/6*a* per layer over six layers, the simulated XRD pattern produces satisfying agreement with the experiment result (Figure S16, Supporting Information). Furthermore, by adding an isotropic strain of 0.4%, the simulated XRD pattern finely reproduces the peak widths as shown in Figure 3a. The as-obtained final structure of the ultrathick layered Ni–F–OH microstructure is given in Figure 3b. The lattice spacing (*d*) based on both the TEM-SAED pattern and HRTEM images (Figure S17, Supporting Information) of

Ni–F–OH was calculated, which are 0.2612 and 0.2600 nm, respectively. We attribute this to the (010) facet of Ni–F–OH based on its triangle symmetry group (Figure 3a), which is perpendicular to the (001) facet as expected.

Scanning transmission X-ray microscope (STXM) spectra of the F and O K-edges in Ni–F–OH were combined with theoretically generated spectra (based on the final relaxed structure). The comparison of the experimental and simulated results is shown in Figure S18 in the Supporting Information. It is noteworthy that this adopted structure, being consistent with all observations, is one of the most optimal ones rather than the only one. It is believed that the structure modelling might be further improved by modifying the distribution and ratio of F and O.

A series of time-dependent experiments are performed to decouple the formation details of Ni–F–OH. As demonstrated by the time-dependent SEM images (Figure 3c), the detectable nanosheets are produced with a reaction time of ≈2.5 h, which become larger and thicker with time, and ultimately achieve high-mass-loading integration onto the substrate with a sub-micrometer thickness (over 700 nm). Moreover, the time-dependent F 1s and Ni 2p X-ray photoelectron spectroscopy (XPS) spectra are compared (Figure 3d). Obviously, the F 1s spectra, which correspond to F[−] in metal-F bonding,^[41,42] follow the same trend as the Ni 2p spectra and the content of F finally reaches a steady state with time (Figure S19, Supporting Information). Combining this with the XRD results, it is found that the diffraction peaks ($2\theta = 19.0^\circ, 34.5^\circ, 36.5^\circ, 47.0^\circ, 60.8^\circ, \text{ and } 64.2^\circ$) related to Ni–F–OH emerge with a reaction time of 2.2 h. The peaks become more and more intense with no emergence of other diffraction peaks after the first 2.5 h (Figure S20, Supporting Information). This is further confirmed by Raman spectra, as shown in Figure 3e. The considerable signal peaks at about 252, 358, and 506 cm^{−1}, related to the Ni–F–OH phase, are observed with the reaction time of 2.5 h, while no additional peaks emerged during the subsequent reaction process. After 8 h of reaction, the Raman mapping images are collected. The images in the regions marked light green, blue and red regions are related to the peaks at 252, 358, and 506 cm^{−1} of the as-made Ni–F–OH phase, respectively. These signals demonstrate the uniform distribution on the carbon fiber with a distinguishable outline, indicative of the intimate and homogenous integration of Ni–F–OH over the carbon substrate.^[43] These results are well-matched with the aforementioned analysis that the dynamic nucleation and growth of ultrathick Ni–F–OH, driven by the dual synergistic effects of NH₄⁺ and F[−], is phase-holding during the whole reaction process.

Further, the sub-micrometer-thickness bimetallic plates were also produced by selective substitution of Ni sites. For example, through the substitution of Ni sites with Co, the bimetallic ultra-thick plate microstructure (the ratio of Co to Ni is 1/3, denoted as Ni₃Co–F–OH) was generated (Figure 4a–c). Here, the as-formed Ni₃Co–F–OH also displays single-crystal characteristics with hexagonal symmetry along (001) plane. It possesses a Ni–F–OH-like crystal structure as shown in the XRD result (Figure 4e,f). The only difference, driven by Co substitution, is the slight negative shift of the typical diffraction peaks (such as these at 2θ of 36.1° and 18.6°), manifesting the lattice expansion and modulation of the host layer and

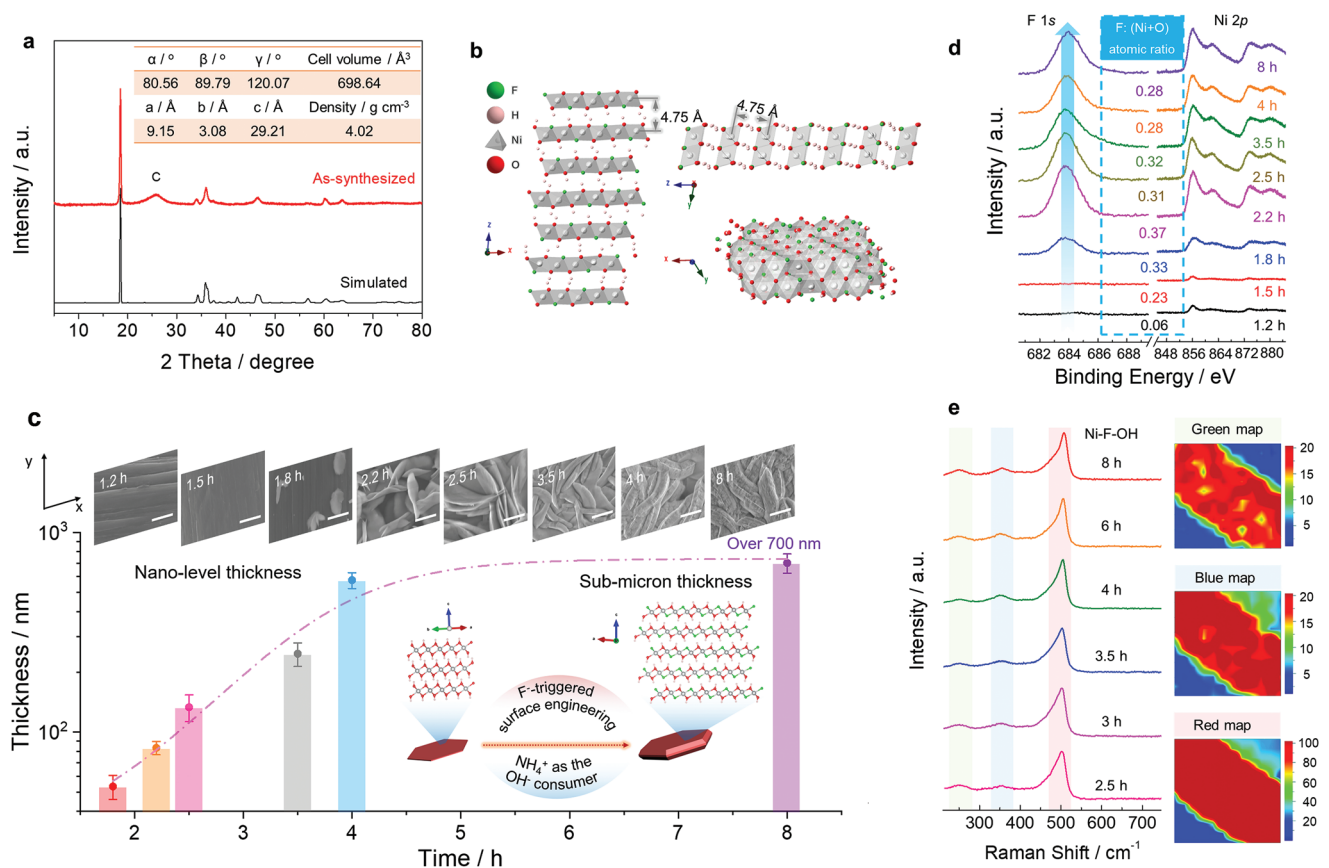


Figure 3. a) A comparison of XRD patterns of Ni-F-OH and its simulated microstructure. b) Finally simulated structure for Ni-F-OH. c–e) Time-dependent experiments of Ni-F-OH: c) SEM images and the variation of the plate thickness with time (Boltzmann fitting is applied to study the tendency, scale bar: 1 μm); d) XPS spectra including F 1s and Ni 2p; and e) Raman spectra for Ni-F-OH samples and Raman mapping images of Ni-F-OH (reaction time of 8 h) in the marked light green, blue, and red regions.

interlayer.^[44,45] Particularly, the tailored Ni-F-OH-like bimetallic single-crystal is extendable and has a big family, evidenced by the formation of Ni₆Ru-F-OH with ultrathick microstructure (Figure S21, Supporting Information).

The tailored ultrathick microstructure is ready to serve as the preactive materials (high-mass-loading precursor) for aqueous energy storage, considering the competitive performances of Ni- and Co-based phosphides or selenides.^[46–48] Figure 4d displays the TEM elemental mapping images of the as-formed phosphorization-treated Ni₃Co-F-OH (Ni₃Co-F-P), where Ni, P, Co, O, and F are homogeneously distributed on the microstructure. XRD analysis shows the generation of the Ni₂P phase with considerable intensity, accompanied by the sharp decrease of the diffraction peak intensity related to Ni₃Co-F-OH (Figure 4e,f), showing that Ni₃Co-F-OH is partially transformed to phosphides. The peak at about 25° is attributed to the (002) plane of the hexagonal graphite carbon structure from our carbon fiber substrate.^[49,50] The XPS spectra demonstrate that the spin-energy separations of Co 2p and Ni 2p are 15.6 and 17.6 eV (Figure S31, Supporting Information), respectively, indicative of the Ni²⁺ and Co²⁺-dominated characteristic of Ni₃Co-F-P.^[51,52] The above results manifest that the tailor-made ultrathick plate superstructures are a versatile family including single metal-/mixed metal-based hydroxides

and their derivatives with advanced properties, holding a great promise to tackle many practical issues in different emerging technologies (Figure 4g).

2.4. Substantial Achievements of the Ultrathick Plate Superstructure for Energy Storage

To investigate the energy-storage performances, the GCD curves of the Ni-F-OH, as well as Ni₃Co-F-OH, were first collected at different current densities (Figure S22a,b, Supporting Information). Both display unsatisfying specific capacities (Figure S22c, Supporting Information) even with ultrathick thickness, as expected. Actually, the developed ultrathick transition-metal hydroxide (such as Ni-F-OH, Ni₃Co-F-OH) can only be used as “preactive” electrode materials, but not directly, i.e., a simple post-treatment of phosphorization or selenylation is needed (Figure S23, Supporting Information). As can be seen in Figure 5a,b, the as-configured Ni₃Co-F-P with a high mass loading up to 25.5 mg cm^{-2} shows reversible charge/discharge capabilities at different current densities, displaying an enhanced areal capacity up to 7144 mC cm^{-2} when compared with that of the as-formed traditional NiCo-based phosphides (Ni₃Co-P, 2668 mC cm^{-2} , Figure S24, Supporting Information)

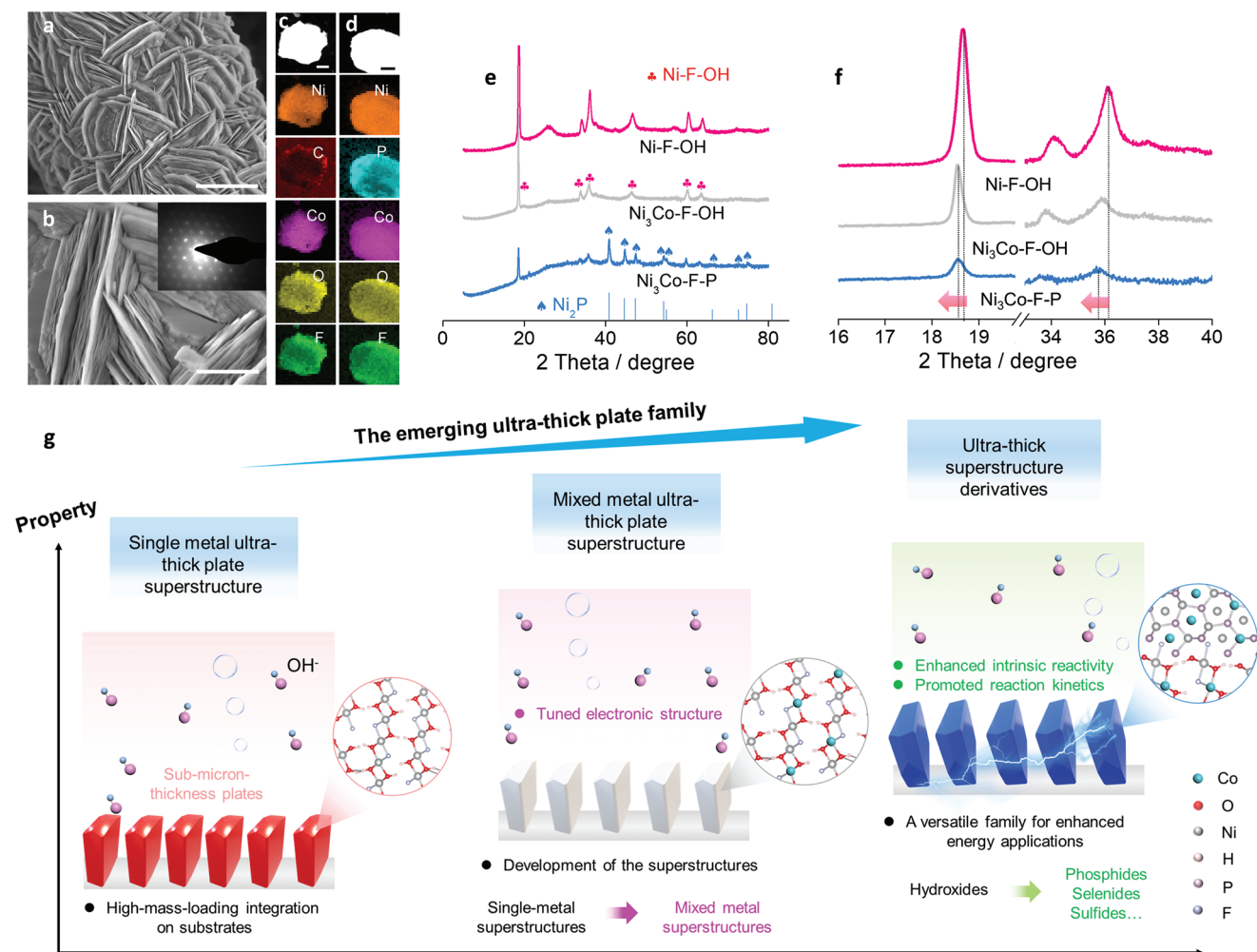


Figure 4. a,b) SEM images of the as-formed $\text{Ni}_3\text{Co-F-OH}$. Scale bar of (a): 4 μm ; scale bar of (b): 1 μm . c,d) TEM elemental mapping images of $\text{Ni}_3\text{Co-F-OH}$ (c) and $\text{Ni}_3\text{Co-F-P}$ (d). Scale bar: 1 μm . e) Comparison of the XRD patterns of the as-formed Ni-F-OH , $\text{Ni}_3\text{Co-F-OH}$, and $\text{Ni}_3\text{Co-F-P}$. f) Magnified XRD patterns of the two regions in (e). g) Scheme illustration of the development of a versatile ultrathick plate family including single metal-/mixed metal-based hydroxides and their derivatives.

as well as a sound volumetric capacity of 223 C cm^{-3} (Figure S25, Supporting Information). Even at a high current density of 50 mA cm^{-2} , a high specific capacity of 5625 mC cm^{-2} can be maintained with a retention rate of 79%.

To understand the origin of its superior performances, we carried out EIS characterization for the ultrathick $\text{Ni}_3\text{Co-F-OH}$ and $\text{Ni}_3\text{Co-F-P}$ electrodes. As shown in Figure S26a (Supporting Information), the $\text{Ni}_3\text{Co-F-OH}$ demonstrates a large semicircle diameter in the high-frequency region, which is attributed to their poor intrinsic conductivity. On the other hand, the $\text{Ni}_3\text{Co-F-P}$ derived from the $\text{Ni}_3\text{Co-F-OH}$ delivers a significantly reduced diameter of the semicircle, indicative of the highly improved conductivity for promoting the charge-transfer dynamics. Moreover, the IR drop was evaluated from the charge/discharge curves at different current densities. As shown in Figure S26b (Supporting Information), the $\text{Ni}_3\text{Co-F-P}$ electrode demonstrates a low IR drop of 12 mV at 4 mA cm^{-2} . As the increase of current density, the values are much lower compared to those of $\text{Ni}_3\text{Co-F-OH}$, indicative of the

fast-kinetic response for highly enhanced charge storage.^[53,54] Furthermore, the electrochemically active surface area (ECSA) of the ultrathick electrode ($\text{Ni}_3\text{Co-F-P}$) was determined and compared with the traditional one assembled with thin plates ($\text{Ni}_3\text{Co-P}$).^[55–58] The total ECSA of the ultrathick electrode is dramatically increased thanks to its increased loading mass (Figure S27, Supporting Information), resulting in the high-packing density of active sites in the unit area. Finally, the cycling measurement of $\text{Ni}_3\text{Co-F-P}$ was carried out at a current density of 50 mA cm^{-2} . It is encouraging that a decent retention rate of up to 82% is achieved after 5000 cycles (Figure S28, Supporting Information). Through the XRD, XPS, and SEM characterizations, the structure evolution was carefully studied and discussed in Figures S29–S31 in the Supporting Information.

This is also the case for selenium-treated $\text{Ni}_3\text{Co-F-OH}$ ($\text{Ni}_3\text{Co-F-Se}$) (mass loading: 27.6 mg cm^{-2}), which displays the highly promoted charge-storage capability (5818 mC cm^{-2}) and rate performance (Figure S32, Supporting Information). The

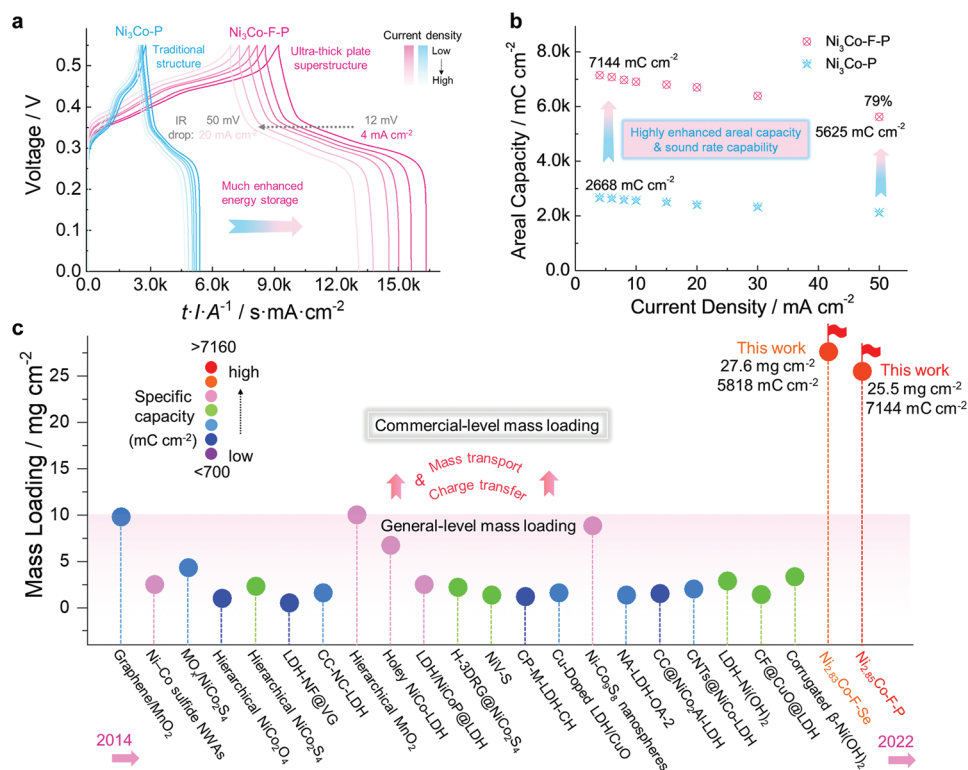


Figure 5. a) Galvanostatic charge/discharge (GCD) curves and b) corresponding areal specific capacities of Ni₃Co-F-P and Ni₃Co-P at different current densities. c) Comparison of the areal specific capacities of our ultrathick plate superstructures and the relative results in the literature.

exact Ni/Co ratios were listed in Table S4 in the Supporting Information. The charge-storage performances of the present ultrathick plate superstructure electrodes were systematically compared with previous studies (Figure 5c; Table S5, Supporting Information). We believe that the as-proposed NH₄⁺ and F⁻ synergistic-modulation strategy, accompanied by simple post-treatment, will allow the development of high-mass-loading self-supporting electrodes with record-level energy storage performances. And we note here that as with most novel strategies, more comprehensive explorations and understandings are highly expected to further boost the development and applications of our strategy. It is predicted that this design route can help close the gap between experimental studies and commercial applications, and attract many efforts for boosting the practical development of energy and material chemistry in the near future.

3. Conclusions

Record-level-thickness (over 700 nm) layered Ni-F-OH plates on carbon substrates, which achieve a superhigh mass loading of 29.8 mg cm⁻² (72% of the whole electrode mass), have been successfully developed. By coupling theoretical simulations with XAFS analysis, we substantiated that the NH₄⁺ and F⁻ modulation produces dual effects. On one hand, the F⁻ enters into the lattice of β-Ni(OH)₂ with superior thermodynamic stability, and tunes the surface energy of (001) plane for high intrinsic activity, thus guiding the formation of ultrathick

layered plates. On the other hand, the NH₄⁺ serves as the consumer of local excessive OH⁻ to restrain the phase separation of Ni-F-OH, ultimately guaranteeing the formation of large and ultra-thick single crystals. Besides the monometallic Ni-F-OH, our strategy was applied to form ultrathick bimetallic plates and their derivatives, producing an attractive transition metal compound family. With a superhigh mass loading, the as-developed ultrathick layered Ni₃Co-F-OH can serve as the preactive materials to achieve an exceptionally high areal capacity of 7144 mC cm⁻² with a sound rate performance (79% at 50 mA cm⁻²), superior to most of the related results in the literature. This NH₄⁺-F⁻-modulation strategy, as the first solution to obtain ultrathick layered plates, successfully breaks the inherent structure limit of 2D layered materials. We believe that, guided by our strategy, these emerging tailored ultrathick 2D materials are able to grow into a rising family, ultimately better meeting practical requirements of energy storage and conversion in the future.

Supporting Information

Supporting Information is available from the Wiley Online Library or from the author.

Acknowledgements

This work was funded by the National Natural Science Foundation of China (NSFC, Nos. 51872035, 51673156, 52202301), the Fundamental

Research Funds for the Central Universities (No. D5000210607) and the Natural Science Basic Research Plan in Shaanxi Province of China (2022)Q-143). W.G. appreciates the great support from Chinese Scholarship Council (No. 201906060084) and China Postdoctoral Science Foundation (2022M722587, 2022TQ0256). This research used resources of Advanced Light Source and Molecular Foundry, DOE Office of Science User facilities under contract DE-AC02-05CH11231. This work was also supported in part by the Advanced Research Projects Agency-Energy Integration and Optimization of Novel Ion Conducting Solids (IONICS) program under Grant No. DE-AR0000774.

Conflict of Interest

The authors declare no conflict of interest.

Author Contributions

W.G., C.D., and M.M. contributed equally to this work. C.Y., J.Q., Q.Z., and J.G. supervised the research. W.G., C.Y., and C.D. designed the experiment and performed material fabrications and analysis. V.Venturi and C.D. examined the implications of surface energy and decomposition enthalpy. V.Venturi performed surface energy and decomposition enthalpy calculations under the supervision of V.Viswanathan. M.M. and Z.G. performed the XAS fitting, simulation and DFT optimization of the Ni-F-OH crystal structure. W.G., F.Y., and X.F. conducted XAFS measurements and carried out electrochemical measurements. C.Y., J.U., and M.M. provided some constructive advice. All authors contributed to the writing of the manuscript.

Data Availability Statement

The data that support the findings of this study are available from the corresponding author upon reasonable request.

Keywords

high-mass-loading, supercapacitors, surface energy, ultrathick plate superstructures, β -Ni(OH)₂

Received: December 12, 2022

Revised: January 9, 2023

Published online: March 22, 2023

- [1] P. Simon, Y. Gogotsi, *Nat. Mater.* **2020**, *19*, 1151.
 [2] H. Sun, J. Zhu, D. Baumann, L. Peng, Y. Xu, I. Shakir, Y. Huang, X. Duan, *Nat. Rev. Mater.* **2018**, *4*, 45.
 [3] A. Noori, M. F. El-Kady, M. S. Rahmanifar, R. B. Kaner, M. F. Mousavi, *Chem. Soc. Rev.* **2019**, *48*, 1272.
 [4] D.-G. Wang, Z. Liang, S. Gao, C. Qu, R. Zou, *Coord. Chem. Rev.* **2020**, *404*, 213093.
 [5] Q. Chen, J. Jin, M. Song, X. Zhang, H. Li, J. Zhang, G. Hou, Y. Tang, L. Mai, L. Zhou, *Adv. Mater.* **2022**, *34*, 2107992.
 [6] D. P. Dubal, O. Ayyad, V. Ruiz, P. Gómez-Romero, *Chem. Soc. Rev.* **2015**, *44*, 1777.
 [7] J. Zhao, H. Cheng, Z. Zhang, Y. Liu, J. Song, T. Liu, Y. He, A. Meng, C. Sun, M. Hu, L. Wang, G. Li, J. Huang, Z. Li, *Adv. Funct. Mater.* **2022**, *32*, 2202063.
 [8] J. Huang, Y. Xiong, Z. Peng, L. Chen, L. Wang, Y. Xu, L. Tan, K. Yuan, Y. Chen, *ACS Nano* **2020**, *14*, 14201.
 [9] S. Liu, L. Kang, J. Hu, E. Jung, J. Zhang, S. C. Jun, Y. Yamauchi, *ACS Energy Lett.* **2021**, *6*, 3011.
 [10] W. Guo, C. Dun, C. Yu, X. Song, F. Yang, W. Kuang, Y. Xie, S. Li, Z. Wang, J. Yu, G. Fu, J. Guo, M. A. Marcus, J. J. Urban, Q. Zhang, J. Qiu, *Nat. Commun.* **2022**, *13*, 1409.
 [11] H. Gao, S. Xin, J. B. Goodenough, *Chem* **2017**, *3*, 26.
 [12] W. Guo, C. Yu, S. Li, J. Qiu, *Energy Environ. Sci.* **2021**, *14*, 576.
 [13] Y. Gogotsi, P. Simon, *Science* **2011**, *334*, 917.
 [14] H.-M. Cheng, F. Li, *Science* **2017**, *356*, 582.
 [15] L. Chang, Y. H. Hu, *Matter* **2019**, *1*, 596.
 [16] Z. Li, S. Gadipelli, H. Li, C. A. Howard, D. J. L. Brett, P. R. Shearing, Z. Guo, I. P. Parkin, F. Li, *Nat. Energy* **2020**, *5*, 160.
 [17] H. Li, Y. Tao, X. Zheng, J. Luo, F. Kang, H.-M. Cheng, Q.-H. Yang, *Energy Environ. Sci.* **2016**, *9*, 3135.
 [18] M. F. El-Kady, Y. Shao, R. B. Kaner, *Nat. Rev. Mater.* **2016**, *1*, 16033.
 [19] Y. Shao, M. F. El-Kady, L. J. Wang, Q. Zhang, Y. Li, H. Wang, M. F. Mousavi, R. B. Kaner, *Chem. Soc. Rev.* **2015**, *44*, 3639.
 [20] W. Guo, F. Yang, C. Yu, Y. Xie, J. Chen, Y. Liu, Y. Zhao, J. Yang, X. Feng, S. Li, Z. Wang, J. Yu, K. Liu, K. Qian, M. Tsige, Q. Zhang, J. Guo, J. Qiu, *Matter* **2021**, *4*, 2902.
 [21] T. Liu, Z. Zhou, Y. Guo, D. Guo, G. Liu, *Nat. Commun.* **2019**, *10*, 675.
 [22] Y. Song, Q. Pan, H. Lv, D. Yang, Z. Qin, M.-Y. Zhang, X. Sun, X.-X. Liu, *Angew. Chem., Int. Ed.* **2021**, *60*, 5718.
 [23] H. Yang, C. Sun, S. Qiao, J. Zou, G. Liu, S. Smith, H. Cheng, G. Lu, *Nature* **2008**, *453*, 638.
 [24] J. Yang, Z. Zeng, J. Kang, S. Betzler, C. Czarnik, X. Zhang, C. Ophus, C. Yu, K. Bustillo, M. Pan, J. Qiu, L. W. Wang, H. Zheng, *Nat. Mater.* **2019**, *18*, 970.
 [25] H.-X. Lin, Z.-C. Lei, Z.-Y. Jiang, C.-P. Hou, D.-Y. Liu, M.-M. Xu, Z.-Q. Tian, Z.-X. Xie, *J. Am. Chem. Soc.* **2013**, *135*, 9311.
 [26] S. Chen, A. Walsh, X.-G. Gong, S.-H. Wei, *Adv. Mater.* **2013**, *25*, 1522.
 [27] B. Wang, N. Novendra, A. Navrotsky, *J. Am. Chem. Soc.* **2019**, *141*, 14501.
 [28] R. A. Flores, C. Paolucci, K. T. Winther, A. Jain, J. A. G. Torres, M. Aykol, J. Montoya, J. K. Nørskov, M. Bajdich, T. Bligaard, *Chem. Mater.* **2020**, *32*, 5854.
 [29] C. Wu, H. Li, Z. Xia, X. Zhang, R. Deng, S. Wang, G. Sun, *ACS Catal.* **2020**, *10*, 11127.
 [30] B. Zhang, K. Jiang, H. Wang, S. Hu, *Nano Lett.* **2019**, *19*, 530.
 [31] S. Dong, W. Shin, H. Jiang, X. Wu, Z. Li, J. Holoubek, W. F. Stickle, B. Key, C. Liu, J. Lu, P. A. Greaney, X. Zhang, X. Ji, *Chem* **2019**, *5*, 1537.
 [32] H. Zhao, Q. Fu, D. Yang, A. Sarapulova, Q. Pang, Y. Meng, L. Wei, H. Ehrenberg, Y. Wei, C. Wang, G. Chen, *ACS Nano* **2020**, *14*, 11809.
 [33] L. Peng, S. Ye, J. Song, J. Qu, *Angew. Chem., Int. Ed.* **2019**, *58*, 9891.
 [34] T.-A. Chen, C.-P. Chuu, C.-C. Tseng, C.-K. Wen, H. S. P. Wong, S. Pan, R. Li, T.-A. Chao, W.-C. Chueh, Y. Zhang, Q. Fu, B. I. Yakobson, W.-H. Chang, L.-J. Li, *Nature* **2020**, *579*, 219.
 [35] Y. Wang, Y. Ma, X.-B. Li, L. Gao, X.-Y. Gao, X.-Z. Wei, L.-P. Zhang, C.-H. Tung, L. Qiao, L.-Z. Wu, *J. Am. Chem. Soc.* **2020**, *142*, 4680.
 [36] S. Li, N. Sharma, C. Yu, Y. Zhang, G. Wan, R. Fu, H. Huang, X. Sun, S. J. Lee, J. S. Lee, D. Nordlund, P. Pianetta, K. Zhao, Y. Liu, J. Qiu, *Adv. Mater.* **2021**, *33*, 2006147.
 [37] T. Kou, S. Wang, J. L. Hauser, M. Chen, S. R. J. Oliver, Y. Ye, J. Guo, Y. Li, *ACS Energy Lett.* **2019**, *4*, 622.
 [38] W. Wang, Y. Wang, R. Yang, Q. Wen, Y. Liu, Z. Jiang, H. Li, T. Zhai, *Angew. Chem., Int. Ed.* **2020**, *59*, 16974.
 [39] X. Zhang, Y. Zhao, X. Jia, Y. Zhao, L. Shang, Q. Wang, G. I. N. Waterhouse, L.-Z. Wu, C.-H. Tung, T. Zhang, *Adv. Energy Mater.* **2018**, *8*, 1702780.
 [40] Y.-J. Wu, J. Yang, T.-X. Tu, W.-Q. Li, P.-F. Zhang, Y. Zhou, J.-F. Li, J.-T. Li, S.-G. Sun, *Angew. Chem., Int. Ed.* **2021**, *60*, 26829.
 [41] S. Wan, J. Qi, W. Zhang, W. Wang, S. Zhang, K. Liu, H. Zheng, J. Sun, S. Wang, R. Cao, *Adv. Mater.* **2017**, *29*, 1700286.

- [42] Q. Huang, T. P. Pollard, X. Ren, D. Kim, A. Magasinski, O. Borodin, G. Yushin, *Small* **2019**, *15*, 1804670.
- [43] Y. Yu, G.-H. Nam, Q. He, X.-J. Wu, K. Zhang, Z. Yang, J. Chen, Q. Ma, M. Zhao, Z. Liu, F.-R. Ran, X. Wang, H. Li, X. Huang, B. Li, Q. Xiong, Q. Zhang, Z. Liu, L. Gu, Y. Du, W. Huang, H. Zhang, *Nat. Chem.* **2018**, *10*, 638.
- [44] D. Zhou, S. Wang, Y. Jia, X. Xiong, H. Yang, S. Liu, J. Tang, J. Zhang, D. Liu, L. Zheng, Y. Kuang, X. Sun, B. Liu, *Angew. Chem., Int. Ed.* **2019**, *58*, 736.
- [45] N. Feng, R. Meng, L. Zu, Y. Feng, C. Peng, J. Huang, G. Liu, B. Chen, J. Yang, *Nat. Commun.* **2019**, *10*, 1372.
- [46] Y. Lin, K. Sun, S. Liu, X. Chen, Y. Cheng, W.-C. Cheong, Z. Chen, L. Zheng, J. Zhang, X. Li, Y. Pan, C. Chen, *Adv. Energy Mater.* **2019**, *9*, 1901213.
- [47] X. Zhao, H. Wan, P. Liang, N. Wang, C. Wang, Y. Gan, X. Chen, Q. Tan, X. Liu, J. Zhang, Y. Wang, H. Wang, H. Wang, *Nano Res.* **2021**, *14*, 2574.
- [48] W. Guo, C. Yu, C. Zhao, Z. Wang, S. Li, J. Yu, X. Tan, Y. Xie, L. Yang, H. Huang, R. Fu, J. Qiu, *Energy Storage Mater.* **2020**, *31*, 172.
- [49] X. Han, X. Tong, G. Wu, N. Yang, X.-Y. Guo, *Carbon* **2018**, *129*, 245.
- [50] S. Li, C. Yu, J. Yang, C. Zhao, M. Zhang, H. Huang, Z. Liu, W. Guo, J. Qiu, *Energy Environ. Sci.* **2017**, *10*, 1958.
- [51] T. Tian, M. Zheng, J. Lin, X. Meng, Y. Ding, *Chem. Commun.* **2019**, *55*, 1044.
- [52] Z. Niu, S. Fan, X. Li, J. Duan, A. Chen, *Appl Catal B* **2023**, *322*, 122090.
- [53] L. Sheng, J. Chang, L. Jiang, Z. Jiang, Z. Liu, T. Wei, Z. Fan, *Adv. Funct. Mater.* **2018**, *28*, 1800597.
- [54] S. Zhang, J. Zhu, Y. Qing, L. Wang, J. Zhao, J. Li, W. Tian, D. Jia, Z. Fan, *Adv. Funct. Mater.* **2018**, *28*, 1805898.
- [55] K. Tian, J. Wang, L. Cao, W. Yang, W. Guo, S. Liu, W. Li, F. Wang, X. Li, Z. Xu, Z. Wang, H. Wang, Y. Hou, *Nat. Commun.* **2020**, *11*, 3884.
- [56] H. Peng, B. Yao, X. Wei, T. Liu, T. Kou, P. Xiao, Y. Zhang, Y. Li, *Adv. Energy Mater.* **2019**, *9*, 1803665.
- [57] X. Gao, X. Liu, D. Wu, B. Qian, Z. Kou, Z. Pan, Y. Pang, L. Miao, J. Wang, *Adv. Funct. Mater.* **2019**, *29*, 1903879.
- [58] B. Chen, X. He, F. Yin, H. Wang, D.-J. Liu, R. Shi, J. Chen, H. Yin, *Adv. Funct. Mater.* **2017**, *27*, 1700795.